




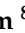




## Article

# Synthesis of One-Dimensional Titanium Oxide Nanowires for Polyvinylidene Fluoride Membrane Optimization

Muhammad Arsalan Dilbraiz<sup>1</sup>, Mohsan Nawaz<sup>1,\*</sup>, Mr. Imtiaz<sup>2</sup>, Pervaiz Ahmad<sup>3</sup>, Sirajul Haq<sup>4,\*</sup>, Zia Ur Rehman<sup>1</sup>, Hameed Ullah<sup>5</sup>, Mayeen Uddin Khandaker<sup>6,7</sup>, Nissren Tamam<sup>8</sup>, Abdelmoneim Sulieman<sup>9</sup> and Majed A. Bajaber<sup>10</sup>

<sup>1</sup> Department of Chemistry, Hazara University, Mansehra 21120, Pakistan

<sup>2</sup> OGDCL, Chanda Oil Field Kohat, Kohat 26000, Pakistan

<sup>3</sup> Department of Physics, University of Azad Jammu and Kashmir, Muzaffarabad 13100, Pakistan

<sup>4</sup> Department of Chemistry, University of Azad Jammu and Kashmir, Muzaffarabad 13100, Pakistan

<sup>5</sup> Department of Chemistry, Islamia College University, Peshawar 25120, Pakistan

<sup>6</sup> Centre for Applied Physics and Radiation Technologies, School of Engineering and Technology, Sunway University, Bandar Sunway 47500, Selangor, Malaysia

<sup>7</sup> Department of General Educational Development, Faculty of Science and Information Technology, Daffodil International University, DIU Rd, Dhaka 1341, Bangladesh

<sup>8</sup> Department of Physics, College of Sciences, Princess Nourah bint Abdulrahman University, P.O. Box 84428, Riyadh 11671, Saudi Arabia

<sup>9</sup> Department of Radiology and Medical Imaging, Prince Sattam bin Abdulaziz University, P.O. Box 422, Al-Kharj 11942, Saudi Arabia

<sup>10</sup> Department of Chemistry, University Faculty of Science, King Khalid University, P.O. Box 9004, Abha 61413, Saudi Arabia

\* Correspondence: mohsannawaz@hotmail.com (M.N.); cii\_raj@yahoo.com (S.H.)



**Citation:** Dilbraiz, M.A.; Nawaz, M.; Imtiaz, M.; Ahmad, P.; Haq, S.; Rehman, Z.U.; Ullah, H.; Khandaker, M.U.; Tamam, N.; Sulieman, A.; et al. Synthesis of One-Dimensional Titanium Oxide Nanowires for Polyvinylidene Fluoride Membrane Optimization. *Crystals* **2022**, *12*, 1164. <https://doi.org/10.3390/cryst12081164>

Academic Editor: Jian-Wei Liu

Received: 28 June 2022

Accepted: 30 July 2022

Published: 19 August 2022

**Publisher's Note:** MDPI stays neutral with regard to jurisdictional claims in published maps and institutional affiliations.



**Copyright:** © 2022 by the authors. Licensee MDPI, Basel, Switzerland. This article is an open access article distributed under the terms and conditions of the Creative Commons Attribution (CC BY) license (<https://creativecommons.org/licenses/by/4.0/>).

**Abstract:** Due to their beneficial characteristics, 1D nanowires have made significant advancements in different realms due to their large surface area, unique surface chemistry, and tunable transport properties. Herein, a comprehensive study of titanium oxide nanowires from titanium (IV) isopropoxide, with the addition of CNTs in the polymeric membrane, has been conducted to form crystals. This method is quite proficient for nanowire synthesis, incorporated with CNTs and polymeric membranes. Carbon nanotubes (CNTs) were used to enhance their properties with polymeric polyvinylidene fluoride PVDF membrane. The concentration ratio of titanium oxide in PVDF membrane was 1, 3, 5, 10, and 15%. The development of titanium oxide nanowires at the nano level shaped, as the emulsion electrospinning created 1D nanowires. The use of an additive makes the membrane more conductive. FT-IR, XRD, EDS, and SEM techniques were used for size, surface geometry, crystalline nature, blend membrane, and thin film composition determination. Thermal Gravimetric Analysis (TGA) analysis shows that weight loss with temperature increases at optimum level.

**Keywords:** synthesis; anatase; titanium oxide; CNTs; surface morphology; nanowires

## 1. Introduction

Nanomaterials have emerged as an exciting class of materials with a wide range of applications in chemistry, physics, the medical field, and many more areas [1–3]. In the last 25 years, scientists have developed nanowires a thousand times thinner than a human hair, which enables new frontiers in medicine, energy, photonics, and computing. Nanowire properties like higher storage and velocity of transmission, the absorption edge of nanoparticles for the blue shift, conductance, increasing mechanical properties, etc. can be easily understood with a theoretical approach and calculation done in a low dimension system [4–8]. 1D nanostructures are ideal systems as compared to 0D and 2D systems to explain transport phenomena at a nanoscale level [9,10]. With low-dimensional systems,

the functional nanostructured arrays for fabrication play a vital role in nanotechnology. The single and multi-walled carbon nano tubes with 1D nanostructures given their versatile and attractive properties for multiple applications [11]. In the field of lithography, many innovative procedures i.e., extreme ultraviolet lithography (EUL) and electron-beam lithography (EBL), limit the cost when the smallest dimension in the circuit is diminished through predetermined masks. Nanowires become an important feature to integrate one dimension (1D) nanostructure, nanocircuit fabrication, magnetic storage information, spintronics, magneto electronics, and magnetic recording in low dimension material synthesis [12]. The surface chemistry and morphology of nanofibers include ZnO, SnO, and TiO<sub>2</sub>, as reported [13–17].

Polyvinylidene fluoride (PVDF) possesses semicrystalline thermoplastic and electroactive polymers with piezoelectric and pyroelectric properties. Due to its thermal ability, high elasticity and chemical resistance, PCDF has many applications in chemical, biochemical and electronic industries for supercapacitors, transducers, sensors, and batteries. PVDF membranes have been extensively used in ultrafiltration and microfiltration for separation purposes [18,19]. PVDF is a thermoplastic engineering material with several applications with a combination of flexibility, low weight, low thermal conductivity, high chemical corrosion resistance, and heat resistance [20,21]. Classical CNTs exhibit some of their very unique properties like high flexibility, low mass density, large aspect ratio (>1000) high tensile moduli, and strengths, and these properties made CNTs a very important and ideal reinforcing agent. The hydrophobic property of CNTs becomes an interesting feature for the absorption of long-chain covalent and non-covalent molecules on the surface. The fabrication of ultrafiltration membranes of PVDF/MWCNTs by phase inversion, however, oxidized MWCNTs with -OH and -COOH functionality enhance the architecture and efficiency of ultra-membrane filtration (UF) membrane.

In the present study, a new approach was used for the synthesis of the polymeric membrane of TiO<sub>2</sub>, and the effects were evaluated on their properties by using additives for the functionalized carbon nanotubes. The interaction of CNTs/PVDF/TiO<sub>2</sub> nanocomposite enhanced the dielectric property and conductivity with an increase in the concentration of CNTs/TiO<sub>2</sub>.

## 2. Materials and Methods

### 2.1. Materials and Methods

Titanium (IV) isopropoxide 97%, *N,N*-dimethylformamide anhydrous 99.8% DMF, acetic acid, and polyvinyl pyrrolidone PVP (C<sub>6</sub>H<sub>9</sub>NO)<sub>n</sub> with a molar mass of 8,000,000 g·mol<sup>-1</sup> were purchased from Sigma-Aldrich, St. Louis, Missouri, United States. polyvinylidene fluoride PVDF and carbon nano tubes were purchased from Sun Nanotechnology.

### 2.2. Preparation of TiO<sub>2</sub> Nanowires

Highly porous TiO<sub>2</sub> nanowires were prepared by a two-step process. About 1.6 mL of titanium isopropoxide was dissolved in 6 mL *N,N*-dimethylformamide anhydrous and stirred till the solution became clear and labeled as solution 1. 1 g Polyvinyl pyrrolidone (PVP) was dissolved in 10 mL anhydrous dimethylformamide and 5 mL ethanol mixture and stirred for 2 h and was labeled as solution 2. Both solutions 1 and 2 were mixed to get a viscous gel-like sample. About 2 mL acetic acid were added dropwise until the solution became clear and ready for the electrospinning process. As with a typical electrospinning process, the spinneret had an inner diameter of 0.6 mm. Grounded aluminum strips (2 cm in width) with parallel gaps of about 1 cm were used as the collectors. A distance of 15 cm and a direct current voltage of 13 kV were maintained between the tips of the spinneret and the collector. During the electrospinning process, the temperature was maintained at 30 °C. After electrospinning, a portion of the obtained TiO<sub>2</sub> nanowires was calcined at 450 °C at a rate of 2 °C per min for 4 h.

### 2.3. Pre and Post Calcination Coupling PVDF Membrane with TiO<sub>2</sub> Nanowires

For the preparation of films, PVDF membranes were coupled with both calcined and non-calcined TiO<sub>2</sub> nanowires. Different mass percent ratios of TiO<sub>2</sub> nanowires (1, 3, 5, 10, and 15%) and PVDF were prepared in DMF solvent. About 1.5 g PVDF were mixed with non-calcined TiO<sub>2</sub> nanowires as fillers in 7 mL DMF solvent and the mixture was stirred vigorously until homogeneous. This homogenous mixture was refluxed for 10 h before the film casting inversion method was applied. The obtained samples were dried at 80 °C and denoted as PVDF/XTO<sub>n</sub>, where X denotes different mass percent ratios of PVDF and 'n' in the subscript stands for the non-calcined TiO<sub>2</sub> nanowires. The same procedure was followed for the coupling of PVDF with calcined TiO<sub>2</sub> nanowires and the obtained samples were denoted as PVDF/XTO<sub>c</sub>, where X denotes different mass percent ratios of PVDF and 'c' in the subscript stands for the calcined TiO<sub>2</sub> nanowires.

### 2.4. Coupling CNT Functionalized PVDF with TiO<sub>2</sub> Nanowires

For the preparation of films, CNT functionalized PVDF was coupled with both calcined and non-calcined TiO<sub>2</sub> nanowires. Different mass percent ratios of TiO<sub>2</sub> nanowires (1, 3, 5, 10, and 15%), functionalized CNTs (-COOH), and PVDF were prepared in DMF solvent. About 1.5 g PVDF were mixed with functionalized CNTs and non-calcined TiO<sub>2</sub> nanowires as fillers in 10 mL DMF solvent and the mixture was stirred vigorously until homogenous. The obtained mixture was refluxed for 10 h before the film casting inversion method was applied. The obtained samples were dried at 80 °C and denoted as PVDF/CNT/XTO<sub>n</sub>, where X denotes different mass percent ratios of PVDF and 'n' in the sub-script stands for the non-calcined TiO<sub>2</sub> nanowires. The same procedure was followed for the coupling of PVDF/CNT with calcined TiO<sub>2</sub> nanowires and the obtained samples were denoted as PVDF/CNT/XTO<sub>c</sub>, where X denotes different mass percent ratios of PVDF and 'c' in the sub-script stands for the calcined TiO<sub>2</sub> nanowires. The experimental detail has been listed in Table 1.

**Table 1.** Composition of PVDF/TiO<sub>2</sub>/MWCNTs nanocomposite with (Wt. %).

Sample	PVDF wt%	MWCNTs wt%	Uncalcined TiO <sub>2</sub> wt%	Sample	PVDF wt%	MWCNTs wt%	Calcined TiO <sub>2</sub> wt%
PVDF/TiO <sub>2</sub> (1)	99	0	1	PVDF/TiO <sub>2</sub> (1)	99	0	1
PVDF/TiO <sub>2</sub> (3)	97	0	3	PVDF/TiO <sub>2</sub> (3)	97	0	3
PVDF/TiO <sub>2</sub> (5)	95	0	5	PVDF/TiO <sub>2</sub> (5)	95	0	5
PVDF/TiO <sub>2</sub> (10)	90	0	10	PVDF/TiO <sub>2</sub> (10)	90	0	10
PVDF/TiO <sub>2</sub> (15)	85	0	15	PVDF/TiO <sub>2</sub> (15)	85	0	15
PVDF/TiO <sub>2</sub> /MWCNTs (1)	99	0.5	0.5	PVDF/TiO <sub>2</sub> /MWCNTs (1)	99	0.5	0.5
PVDF/TiO <sub>2</sub> /MWCNTs (3)	97	1.5	1.5	PVDF/TiO <sub>2</sub> /MWCNTs (3)	97	1.5	1.5
PVDF/TiO <sub>2</sub> /MWCNTs (5)	95	2.5	2.5	PVDF/TiO <sub>2</sub> /MWCNTs (5)	95	2.5	2.5
PVDF/TiO <sub>2</sub> /MWCNTs (10)	90	5	5	PVDF/TiO <sub>2</sub> /MWCNTs (10)	90	5	5
PVDF/TiO <sub>2</sub> /MWCNTs (15)	85	7.5	7.5	PVDF/TiO <sub>2</sub> /MWCNTs (15)	85	7.5	7.5
Sample PVP wt%	10						
		TiO <sub>2</sub> wt%	90				

### 2.5. Characterization

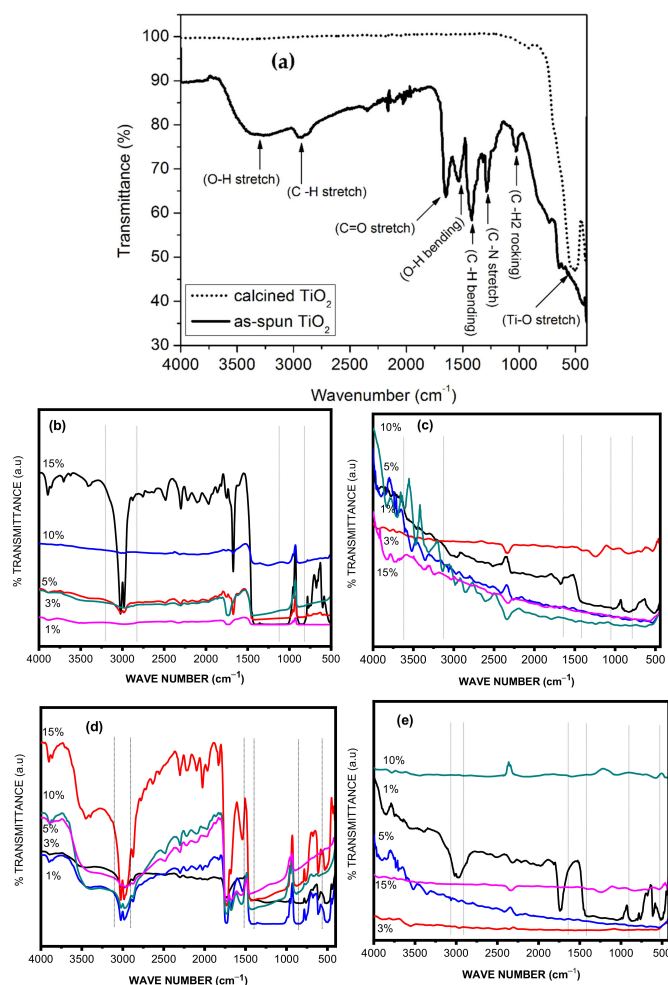
X-ray diffractometric analysis were recorded on a STOE Germany THETA-THETA diffractometer to study the crystal structure and atomic spacing. The anode material was made of Cu, the scan step time was 0.4000 s, and the receiving slit size was 0.3000 mm at 25 °C. The IR spectra in the range of 4000–400 cm<sup>-1</sup> were measured using the FTIR spectrometer of Thermo Fisher Scientific Waltham, MA, USA, (Spectrum 100 series). Scattering electron microscopic images were recorded on JEOL JSM-6490A. Electron diffraction spectroscopy was performed on JEOL model JED-2300 analysis station. Tensile strength and elongation at break were measured using an MTS testing machine with an initial speed of 100 mm/min. The average of five measurements along with their standard deviation was taken.

## 3. Results

### 3.1. FTIR Analysis

The FTIR spectra of TiO<sub>2</sub> nanowires are shown in Figure 1a–e. The band positioned around 487 cm<sup>-1</sup> is due to the Ti-O-Ti stretching vibration of the tetragonal TiO<sub>2</sub>. The

figure shows that the peaks at 874 and 1100  $\text{cm}^{-1}$  are attributed to the middle and strong stretching vibrations of Ti-O-Ti, respectively. The strong absorption peaks at around 3400 and 1630  $\text{cm}^{-1}$  are assigned to O-H stretching and H-O-H bending vibrations of physically adsorbed water molecules [22]. The FTIR results of PVDF/ $\text{XTO}_n$ , PVDF/ $\text{XTO}_c$ , PVDF/CNT/ $\text{XTO}_n$ , and PVDF/CNT/ $\text{XTO}_c$  that show characteristic peaks at 1375, 1176, and 973  $\text{cm}^{-1}$  are respectively assigned to C-H deformation, C-F stretching and Ti-OH stretching [15–17]. The FTIR spectra reveal the spectra of  $\text{TiO}_2$  nanowires in Figure 1a, whereas the FTIR spectrum in Figure 1b,c shows the effect of  $\text{TiO}_2$ /PVDF 1%, 3%, 5%, 10%, and 15% before and after calcination, respectively. The nanowires of  $\text{TiO}_2$ /PVDF composite show the absorbance on wave number ( $\text{cm}^{-1}$ ). As the concentration of composite increases, the absorbance of the materials becomes variable due to the increase in the concentration of the PVDF polymer. The band position between 400 to 1100  $\text{cm}^{-1}$  expressed the stretching vibration of  $\text{TiO}_2$  and 1400 to 3500  $\text{cm}^{-1}$  shows the organic peaks of the PVDF polymer [23] whereas after calcination the organic peaks were removed. Moreover, Figure 1d,e reveals the FTIR spectrum of  $\text{TiO}_2$ /CNTs/PVDF 1%, 3%, 5%, 10% and 15% before and after calcination, respectively. The absorbance peaks were determined with the increase in the concentration of the PVDF polymer. The absorbance peak from 1600 to 3500  $\text{cm}^{-1}$  shows the organic peaks of the thin sheet, whereas the one from 400 to 1100  $\text{cm}^{-1}$  indicates that the  $\text{TiO}_2$  stretching vibration and CNTs peaks were observed. After calcination, organic and CNTs peaks were removed as indicated in the spectrum.



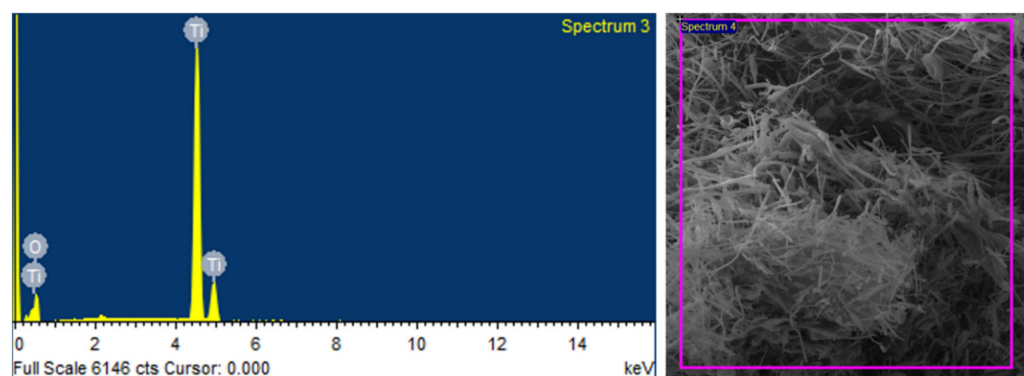
**Figure 1.** (a) FTIR spectrum of the as-spun  $\text{TiO}_2$  nanowires, (b,c) shows  $\text{TiO}_2$ /PVDF films prepared with 1 wt%, 3wt%, 5wt%, 10 wt% and 15 wt% concentration of the as-spun and calcined  $\text{TiO}_2$  nanowires, (d,e) shows as-spun and calcined  $\text{TiO}_2$ /f-MWCNTs/PVDF films prepared with 1 wt%, 3wt%, 5wt%, 10 wt%, and 15 wt% concentration f-MWCNTs.

### 3.2. EDS Analysis

The existence and composition of the synthesized TiO<sub>2</sub> nanowires were also confirmed by the energy dispersive x-ray spectroscopy and the recorded EDX spectrum is given in Figure 2 which shows the peaks of titanium and oxygen on the left-hand side while the specific area from where the EDX spectrum was obtained is given. It is clear from the EDX spectrum that titanium and oxygen are the only elements present in the spectrum and no other peaks have been detected confirming that no impurities are present and the formation of TiO<sub>2</sub> has successfully taken place. The elemental composition by weight percent (Wt%) and atomic percent (At%) is given in Table 2.

**Table 2.** Elemental composition of TiO<sub>2</sub> nanowires by weight% and Atomic%.

Element	Weight%	Atomic%
O K	33.46	60.09
Ti K	66.54	39.91
Totals	100.00	



**Figure 2.** EDX spectrum of the TiO<sub>2</sub> nanowires.

### 3.3. SEM Analysis

The scanning electron microscopy of the resulting TiO<sub>2</sub> nanowires was done to study the morphology of the obtained nanowires before and after calcination. The SEM micrographs of the as-spun nanowires (pre-calcined nanowires) are given in Figure 3a–g at low and high magnifications, respectively. The morphology of the as-spun nanowires looks very smooth and compact at this stage. The SEM micrographs of the TiO<sub>2</sub> nanowires obtained after calcination are given in Figure 3c,d captured at two different magnifications, and Figure 3e–g shows the overall as-spun nanowires at high and low magnifications. The morphology of the calcined nanowires looks a bit rough, and the size has shrunk due to the removal of the solvent and polymer content. The SEM images of TiO<sub>2</sub> nanowires with wire sizes range from 500 nm to 5 µm. The wire size is regular in structure with aligned characteristics of 1D nanostructures and confirms the geometry of TiO<sub>2</sub> from XRD. The obtained nanowires are several micrometers in length and have a diameter between 150–250 nm.

Figure 4 shows the SEM images of XPVDF/TO<sub>n</sub> which are smooth and porous in morphology. It is clear that for the SEM images in the range of 10–50 the morphology becomes more and smoother as the amount of PVDF increases. The distribution of the as-spun TiO<sub>2</sub> nanowires in the PVDF films/membranes was revealed by the scanning electron micrographs. Figure 4a–e shows the cross-sectional SEM of TiO<sub>2</sub>/PVDF nanocomposite films obtained at different magnifications. In Figure 4a,b, some white spots are visible in the given SEM which are from the TiO<sub>2</sub> nanowires. Figure 4c–e gives a closer look at the composite films showing a very homogenous distribution of the TiO<sub>2</sub> nanowires across the PVDF matrix without any agglomeration.

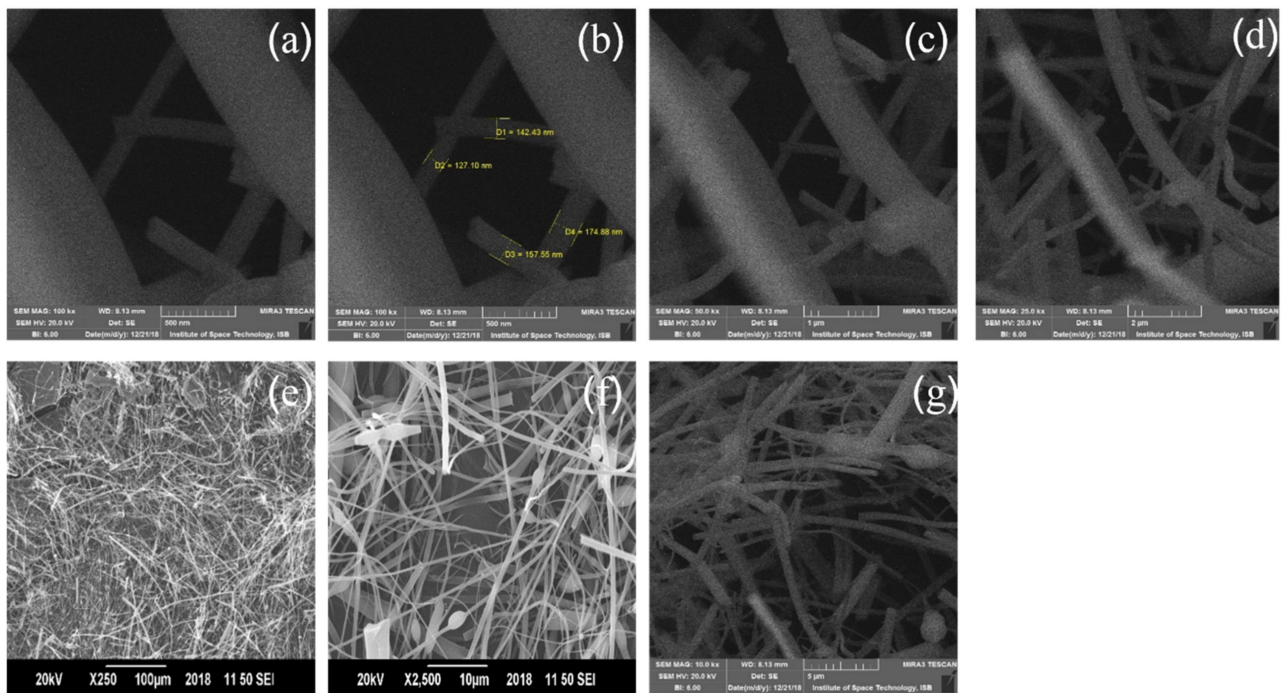


Figure 3. (a–g) SEM images of TiO<sub>2</sub> nanowires.

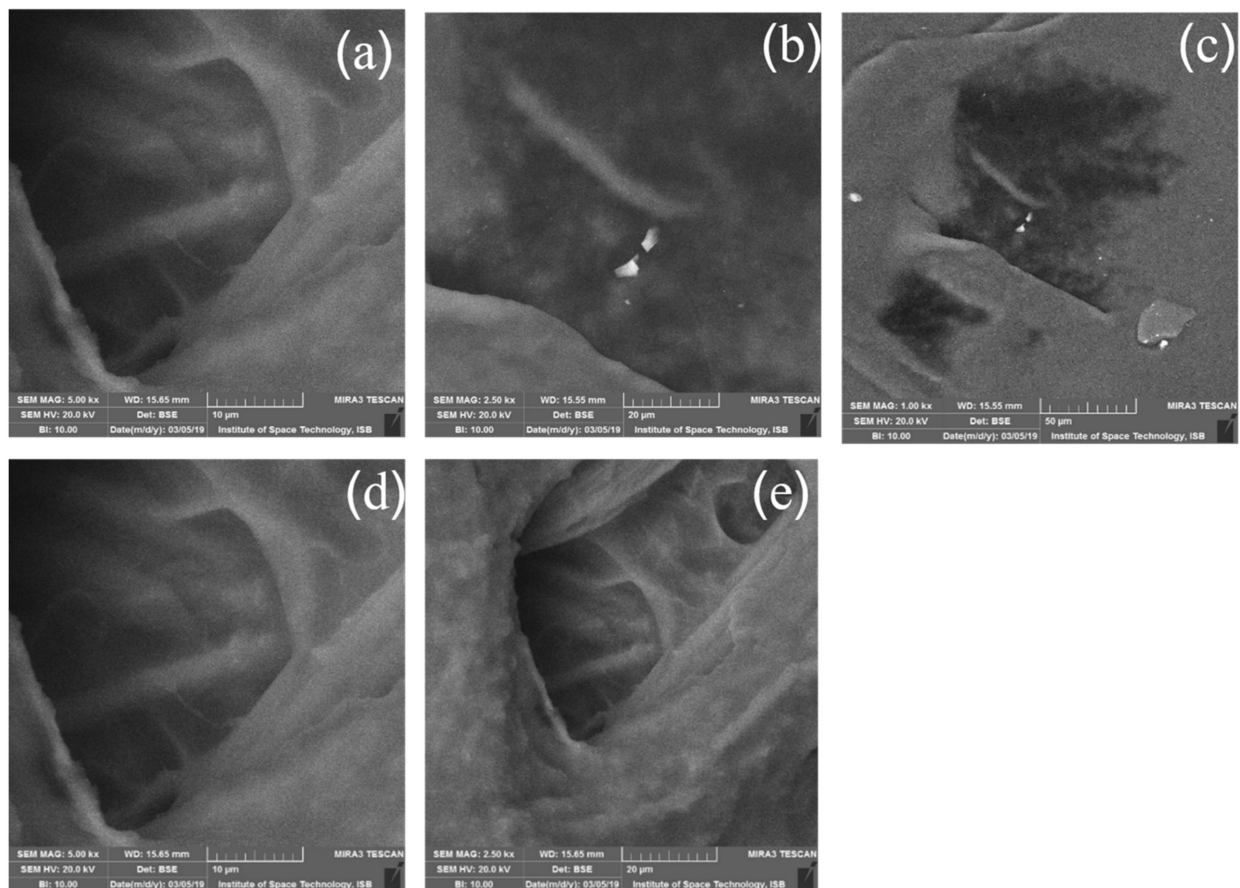
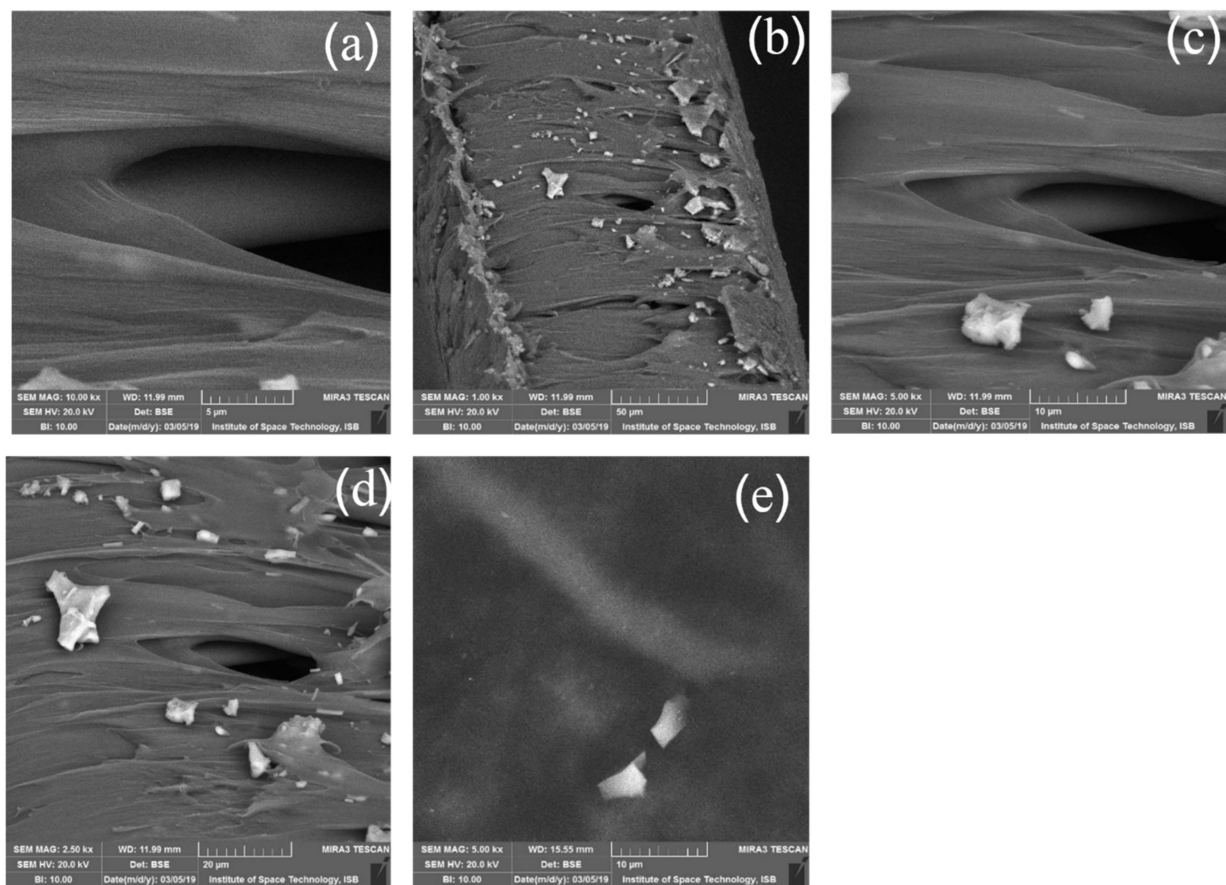


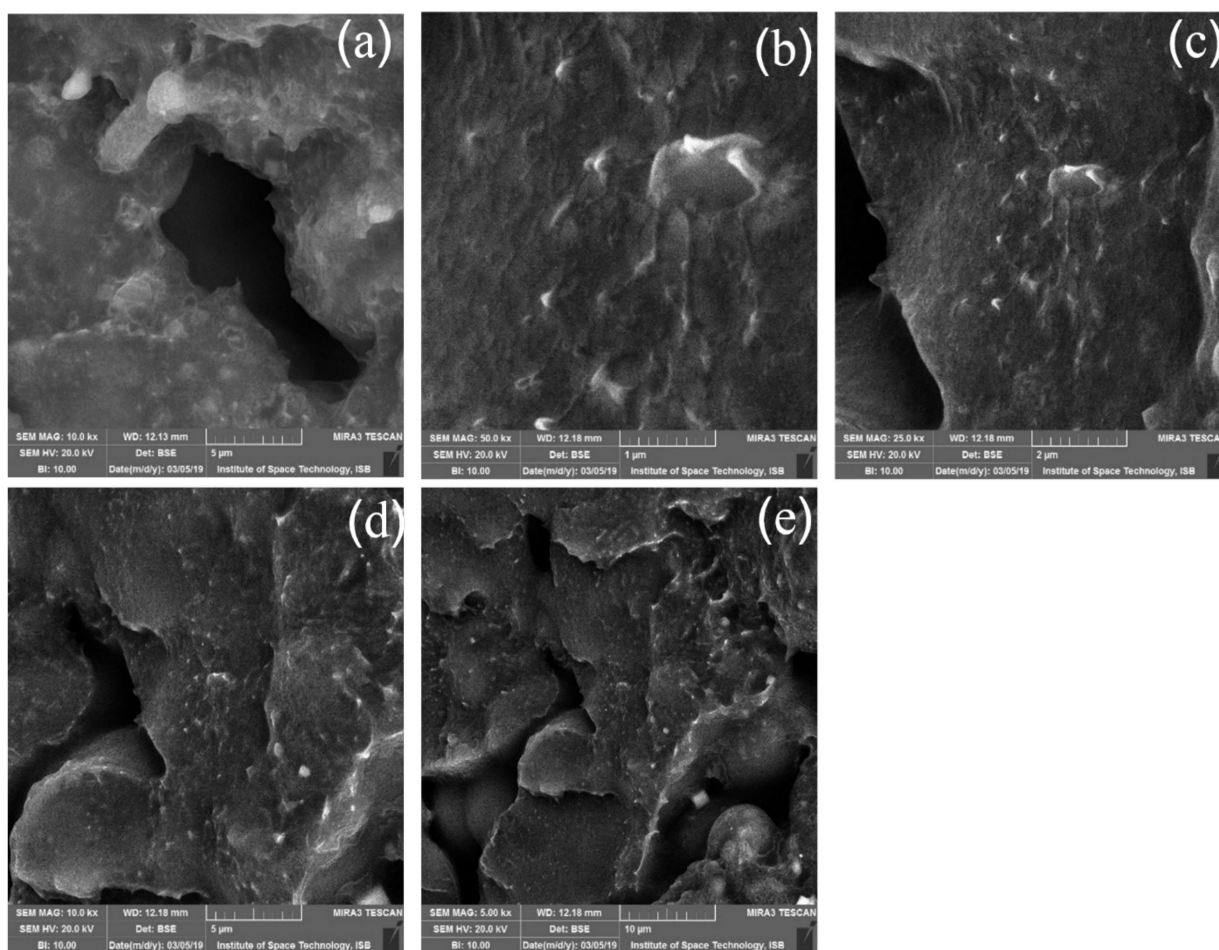
Figure 4. SEM images of series (1% (a), 3% (b), 5% (c), 10% (d), 15% (e)) before calcined TiO<sub>2</sub> nanowires membrane.

The scanning electron micrographs (SEM) obtained for the calcined  $\text{TiO}_2/\text{PVDF}$  nanocomposite films are shown in Figure 5a–e. These SEM provides a cross-sectional view of the microstructure of the  $\text{TiO}_2/\text{PVDF}$  composite membranes showing the chemistry and distribution of the nanofillers of  $\text{TiO}_2$  nanowires in the PVDF matrix. The cross-sectional view at low resolution shows the breakage of the surface and some voids. At higher resolution, the one-dimensional  $\text{TiO}_2$  nanowires have aligned themselves in a longitudinal way with the PVDF matrix and show a very uniform distribution in the PVDF matrix. Figure 5c–e shows SEM images of XPVDF/ $\text{TO}_c$  samples and the morphology is relatively more porous compared to non-calcined samples. The  $\text{TiO}_2$  nanowires are found scattered on the surface of the PVDF. Since calcination increases the crystallinity of the samples, more visible  $\text{TiO}_2$  nanowires are seen scattered on the surface of the PVDF membrane. The whole morphology of the images is in the range of 5–50  $\mu\text{m}$ .



**Figure 5.** SEM images of series (1% (a), 3% (b), 5% (c), 10% (d), 15% (e)) after calcined  $\text{TiO}_2$  nanowires membrane.

The surface morphology of  $\text{TiO}_2/\text{f-MWCNTs}/\text{PVDF}$  nanocomposite films in which the f-MWCNTs were also studied with the SEM to look for the surface study and appearance of the nanofillers in the PVDF matrix. Figure 6a–e shows the SEM of the  $\text{TiO}_2/\text{f-MWCNTs}/\text{PVDF}$  which were obtained from the fracture cross-section of these films. It can be seen that the added nanofillers of both  $\text{TiO}_2$  and f-MWCNTs are uniformly embedded in the PVDF matrix and show a compact surface. Some white nanoparticles attached to the PVDF matrix can also be seen. Conversely, Figure 5c–e shows white indications that may lead toward the head of 1D  $\text{TiO}_2$  nanowires whose tails are dipped and dispersed vertically in the PVDF matrix as the nanowires possess a high aspect ratio. Figure 6a–e shows the SEM images of pre-calcined XPVDF/ $\text{CNT}/\text{TO}_n$  and XPVDF/ $\text{CNT}/\text{TO}_c$  samples with more high porosity and more visible  $\text{TiO}_2$  nanowires of a relatively small range between 1–10  $\mu\text{m}$ .



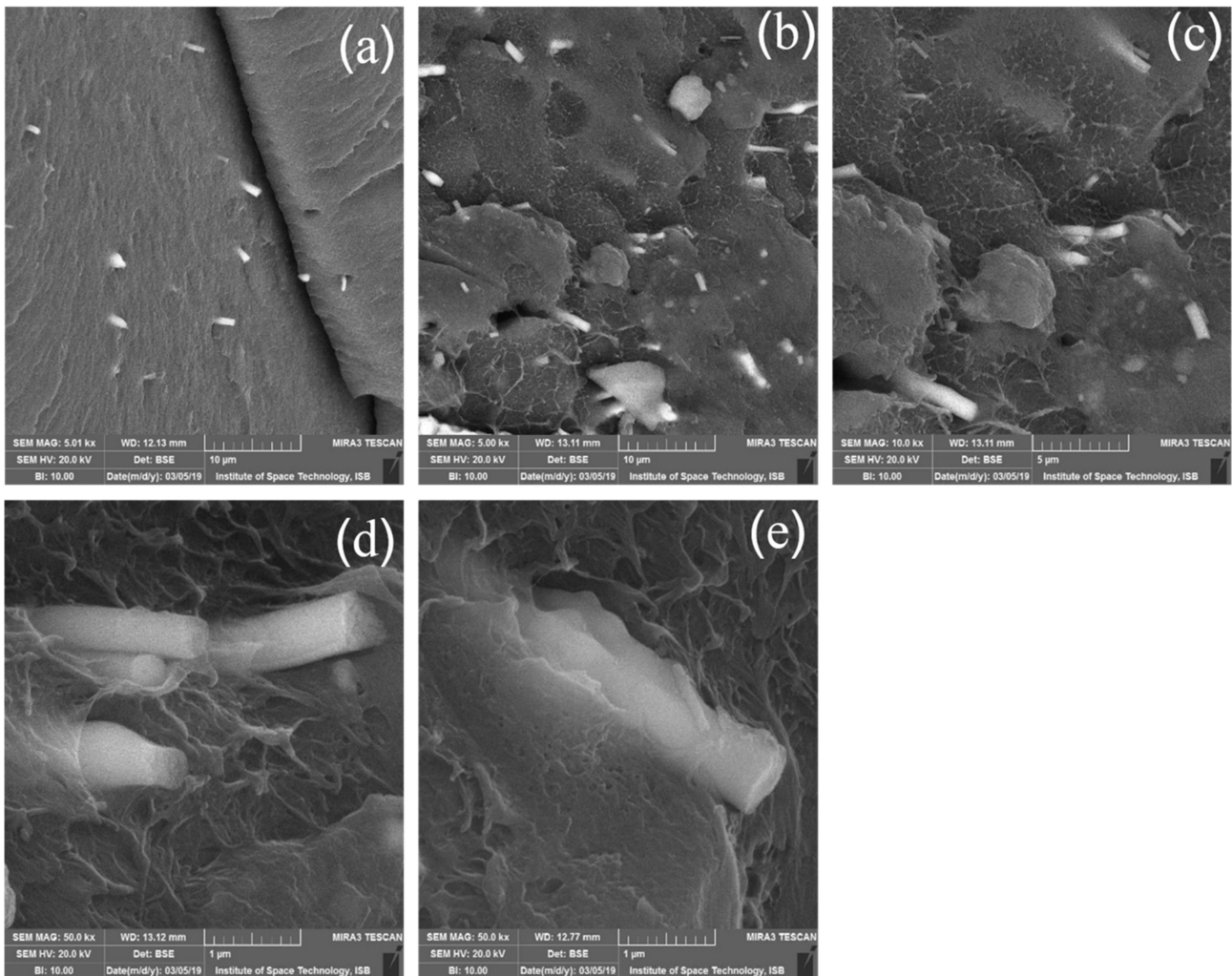
**Figure 6.** SEM images of series (1% (a), 3% (b), 5% (c), 10% (d), 15% (e)) before calcined TiO<sub>2</sub> nanowires with CNTs blend membrane.

The surface morphology of the nanocomposite films prepared by solution casting of as-spun TiO<sub>2</sub>/f-MWCNTs/PVDF was studied by the SEM to see the distribution of the nanofillers in the polymer matrix. Figure 7a–e show the post-calcinated cross-section SEM micrographs of the nanocomposite at a low and high resolution where one can see the dispersion of MWCNTs and TiO<sub>2</sub> nanowires in the PVDF matrix with morphology. However, due to the one-dimensionality and very thin size of MWCNTs, they have covered the whole surface of the PVDF matrix. It is the good dispersibility and directionality of the nanofillers which play a role in the alignment of the PVDF structure which results in phase transformation (from  $\alpha$  to  $\beta$ ) on one hand, and on the other hand it provides good thermal stability to the matrix when heated. In Figure 7c–e the standalone nanowires of the as-spun TiO<sub>2</sub> nanowires can also be seen in the given micrographs, which also strengthen the thermal stability of the matrix and provide additional stability.

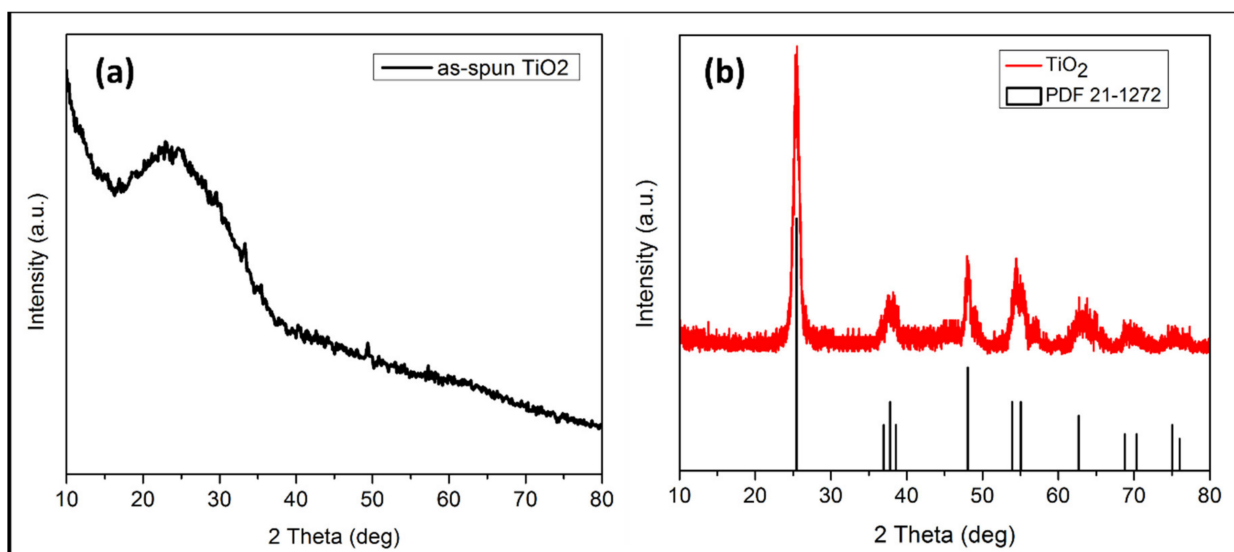
### 3.4. XRD Analysis

Figure 8, matches the XRD pattern of TiO<sub>2</sub> nanowires named Anatase (PDF reference code 01-075-1537). The X-ray diffractions clear the crystallinity of the compound gives unit cell indication and illustrate the TiO<sub>2</sub> anatase phase pattern. The *h*, *k*, and *l* values of the crystal are (112) and (200) peaks, respectively [23]. The diffraction pattern TiO<sub>2</sub> exhibits at 25° and 45°, indicating the strong diffraction pattern of anatase phase TiO<sub>2</sub>.



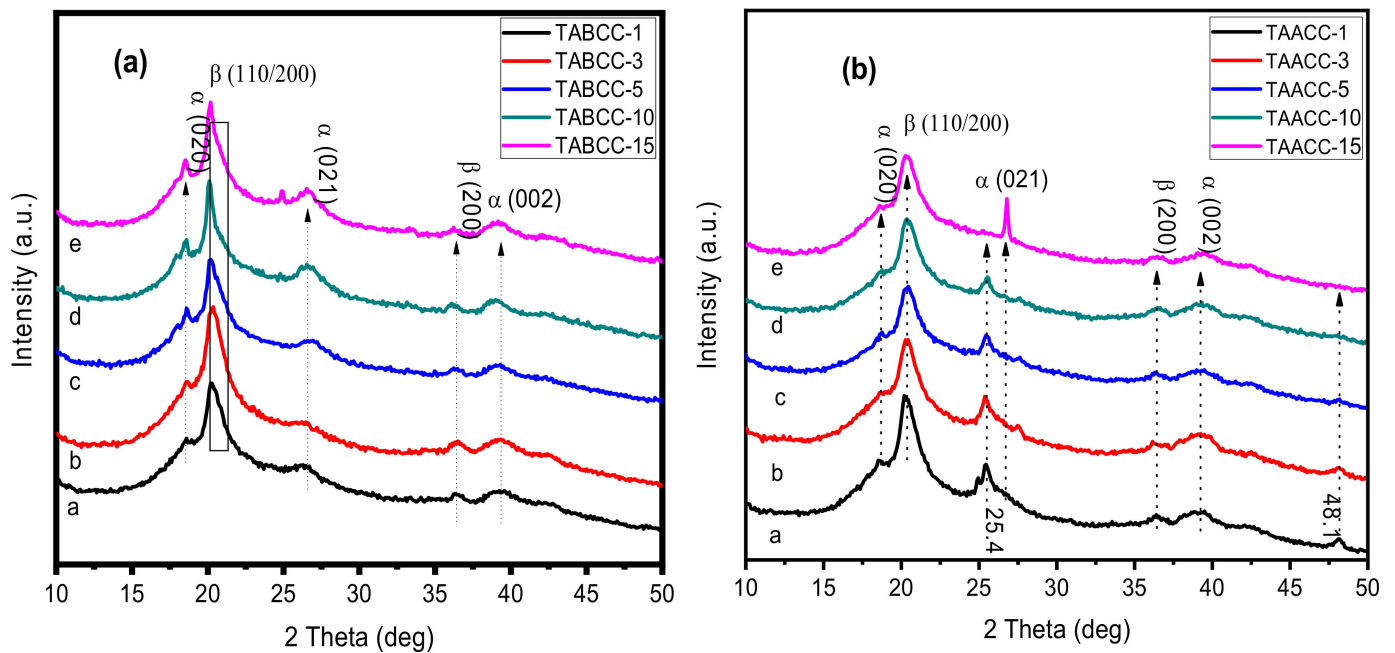


**Figure 7.** SEM images of series (1% (a), 3% (b), 5% (c), 10% (d), and 15% (e)) after calcined TiO<sub>2</sub> nanowires with CNTs blend membrane.



**Figure 8.** XRD diffraction patterns of titanium oxide nanowires: (a) as spun TiO<sub>2</sub> and (b) anatase TiO<sub>2</sub>.

In Figure 9a, matches the XRD pattern of TiO<sub>2</sub> nanowires name as Anatase (PDF reference code 01-075-1537). The X-ray diffractions clear the crystallinity of the compound gives unit cell indication and illustrate the TiO<sub>2</sub> anatase phase pattern. The h, k, and l value of the crystal is (101) and (200) peaks, respectively [23]. The diffraction pattern TiO<sub>2</sub> is exhibited at 25° and 45°, indicating the strong diffraction pattern of anatase phase TiO<sub>2</sub>. The series (1%, 3%, 5%, 10%,15%) reveals the crystallinity of TiO<sub>2</sub> structure with diffraction pattern and exhibits an angle 2θ = 25° and 2θ = 45° with h, k, and l values (101) and (200) respectively.

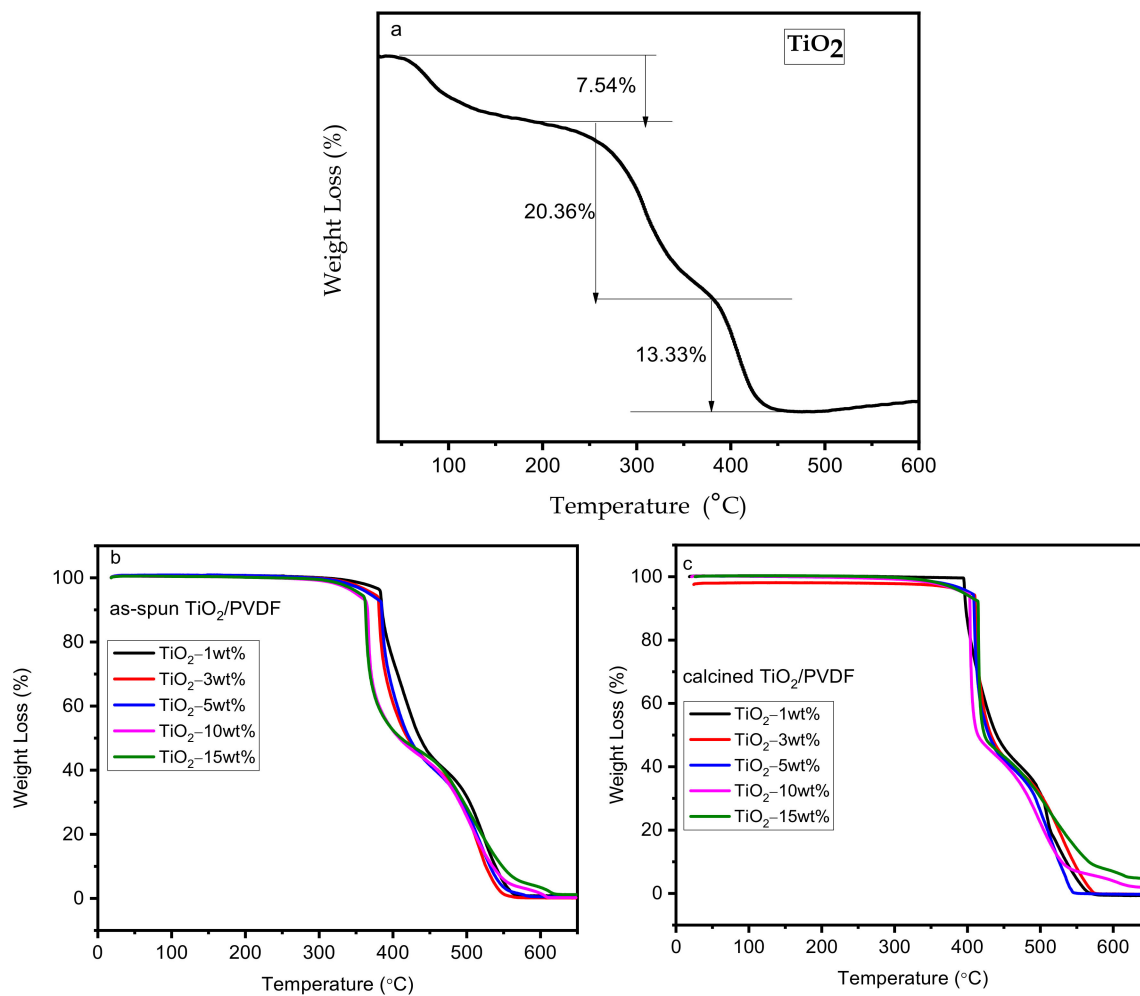


**Figure 9.** (a) XRD analysis of series (1% (a), 3% (b), 5% (c), 10% (d), and 15% (e)) after calcined TiO<sub>2</sub> nanowires with blend membrane (b) after calcined TiO<sub>2</sub> nanowires with CNTs blend membrane.

Figure 9b matches the XRD pattern of TiO<sub>2</sub> nanowires named as Anatase (PDF reference code 01-075-1537). The X-ray diffractions clear the crystallinity of the compound gives unit cell indication and illustrate the TiO<sub>2</sub> anatase phase pattern. The h, k, and l value of the crystal are (101) and (200) peaks, respectively [24]. The diffraction pattern TiO<sub>2</sub> is exhibited at 25° and 45°, indicating the strong diffraction pattern of anatase phase TiO<sub>2</sub>. The series (1%, 3%, 5%, 10%,15%) reveals that the crystallinity of the TiO<sub>2</sub> structure with diffraction pattern exhibits an angle 2θ = 25° and 2θ = 45° with h, k, and l values of (101) and (200), respectively.

### 3.5. Thermal and Mechanical Stability

The typical thermogravimetric (TG) curve for non-calcined TiO<sub>2</sub> nanowires illustrated in Figure 10a shows three steps. The first step of approximately 7.54% mass loss is found in the range of 20–110 °C. The second substantial mass loss of approximately 20.36% appears between 110 and 370 °C and can be attributed to the removal of water molecules and organic material as well. The third mass loss of approximately 13.33% appears between 370 to 450 °C, indicating the removal of the PVP organic template to form nanowires. There are weak exothermic peaks observed and they are related to the slow transformation of the anatase phase of TiO<sub>2</sub> to the rutile phase at high heating.



**Figure 10.** TGA analysis concerning weight loss and temperature increases.

The typical thermogravimetric (TG) curve shown in Figure 10b shows three steps. The first step is approximately 6.54% mass loss from 350 to 410 °C. The second substantial mass loss is approximately 22.63% between 410 and 480 °C and can be allocated for water molecules removal from the hydroxyls on titanium atoms and organic material as well. For the temperature ranges from 480 to 550 °C, there is a mass loss of approximately 10.12%, which indicates the removal of the PVDF organic template to form nanowires. From this, the organic template can be removed from fibrous material to form nanowires upon calcination at 550 °C. There are weak exothermic peaks that are observed in the differential scanning calorimetry (DSC) measurement. It reveals the slow transformation of the anatase phase of TiO<sub>2</sub> to the rutile phase as with the pattern involved with the series (1%, 3%, 5%, 10%, and 15%).

Similarly, the typical thermogravimetric (TG) curve in Figure 10c shows three steps. The first step shows an approximately 5.58% mass loss from 350 to 410 °C. The second substantial mass loss of approximately 23.26% between 410 and 470 °C can be allocated to the removal of water molecules. The temperature ranges from 470 to 550 °C, and there is a mass loss of approximately 12.44%, which indicates the removal PVDF organic template to form nanowires. This indicates the collection of nanowires of prescribed material of TiO<sub>2</sub> calcinated at 550 °C. There are weak exothermic peaks that are observed in the differential scanning calorimetry (DSC) measurement. It reveals the slow transformation of the anatase phase of TiO<sub>2</sub> to the rutile phase as with the pattern involved with the series (1%, 3%, 5%, 10%, and 15%).

Mechanical attributes are vital in industrial membrane applications for long-term performance stability. As a result, data on membrane tensile strength and elongation ratio at break were determined. Table 3 shows the results of the membranes' mechanical strength tests. The mechanical strength of membranes was improved as TiO<sub>2</sub> nanowire content levels were increased. The tensile strength of the membrane increased from 1.57 MPa to 2.19 MPa with the addition of TiO<sub>2</sub> nanowires from 1 wt.% to 15 wt.%, while the elongation ratio increased from 36.91% to 59.01 wt.%. The tensile strength increased from 1.57 MPa to 2.19 MPa with the addition of TiO<sub>2</sub> nanoparticles from 1 to 15 wt.% percent, while the elongation ratio increased from 35.71% to 56.12%. This suggested that inserting TiO<sub>2</sub> nanowires could join polymeric chains while also increasing their stiffness and elasticity. As a result, more energy was required to break the link between TiO<sub>2</sub> nanowires and PVDF, and the hybrid membrane mechanical strength and elongation ratio both improved.

**Table 3.** Mechanical stability of PVDF/TiO<sub>2</sub> nanocomposites.

Sample ID	Tensile Strength	Elongation at Break
TA	1.57 ± 3.9	35.71 ± 3.7
TA-1	1.61 ± 4.3	44.31 ± 3.2
TA-2	1.70 ± 3.1	45.81 ± 3.2
TA-3	1.97 ± 2.7	50.04 ± 2.5
TA-4	2.04 ± 2.2	53.55 ± 2.6
TA-5	2.19 ± 2.3	56.12 ± 2.1

### 3.6. Dielectric Constant

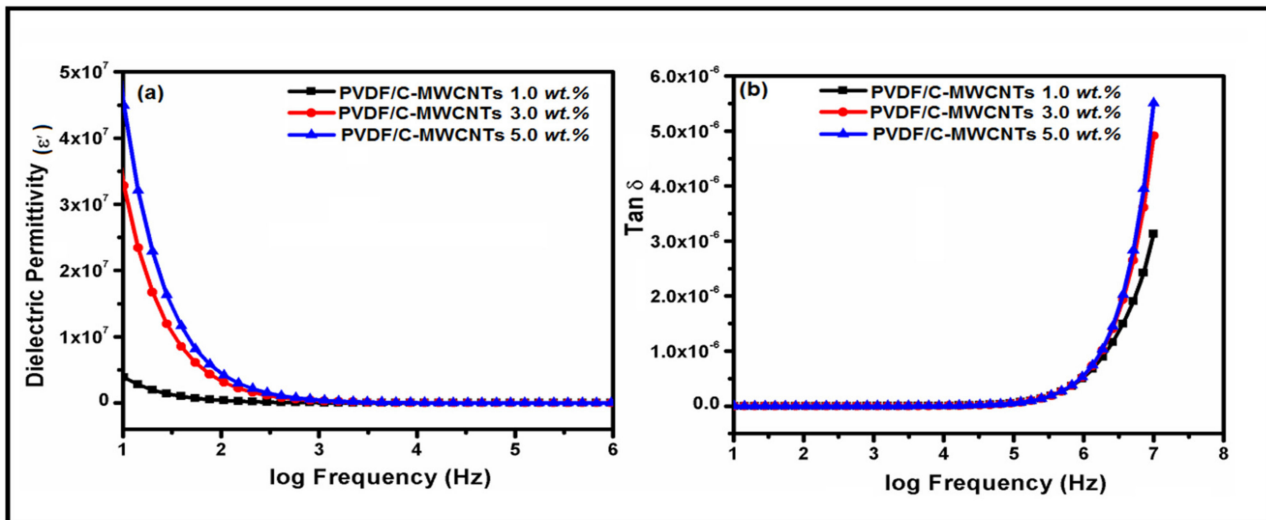
The dielectric permittivity of PVDF/f-MWCNTs/TiO<sub>2</sub> was measured in the range of  $1.0 \times 10^1$ – $1 \times 10^7$  Hz at room temperature. The results reveal that dielectric permittivity has increased appreciably. The interface of reinforcement of functionalized MWCNTs and the matrix of PVDF with the addition of TiO<sub>2</sub> have strong interfacial interaction. There are two factors involved in the enhancement of dielectric permittivity of MWCNTs/TiO<sub>2</sub>/PVDF. One is the combined effect of reinforcement, especially with loading content, and the other is the polymeric chain. The resistance of the charge carrier at the interface with the result of Maxwell-Wagner Sillar effect (MWS). Whereas MWS effect established the collection of charge at interface point when current flows acrosses. The material possesses different relaxation time ( $\tau$ ), equation as follows ( $\tau = \epsilon/\sigma$ ),  $\epsilon$  and  $\sigma$  expressed the dielectric permittivity and conductivity of the respective materials within the composite. The relaxation time of PVDF is very high as compared to MWCNT [24].

In composite material with the addition TiO<sub>2</sub> nanowires to C-MWCNTs/PVDF, the MWS effect is strengthened by the electrophilic fluorine (F) of PVDF. The F attracts the delocalized electron of MWCNTs at the interface led to an established donor-acceptor complex between the interface of PVDF and MWCNTs with TiO<sub>2</sub>. The large surface area of MWCNTs plays a vital role in the enhancement of the MWS effect during formation of a nanoscale structure with the insulating interface of PVDF.

The dielectric permittivity measured at frequency of  $1 \times 10^2$  Hz with a 1%, 3% and 5% C-MWCNT/TiO<sub>2</sub> are  $3.66 \times 10^5$ ,  $3.10 \times 10^6$ , and  $4.17 \times 10^6$ , respectively. The dielectric permittivity response of PVDF was observed to decrease within the frequency range between  $10^1$ – $10^3$ Hz. The dielectric permittivity value is enhanced with the addition of TiO<sub>2</sub> and reached its optimum level as the quantity increases. Therefore, upon concentration that lies within the vicinity of percolation threshold. In this reinforcement concentration there is strong interfacial interaction between functionalized MWCNTs, TiO<sub>2</sub>, and PVDF along with an enhanced MWS effect. The concentration of dielectric permittivity was further enhanced by an increase in interfacial interaction due to an increase in distance between the insulating PVDF and the MWCNTs [25,26]. This can also be expressed by the attributed interfacial polarization between the polymeric matrix and the high  $\beta$ -phase of the polymer with the interaction of nanowires and functionalized MWCNTs [27]. This sequenced increase in the dielectric permittivity in the lower frequency range was based on

the mini-capacitor principle. Alongside, the dielectric permittivity of PVDF was observed to decrease sharply with the frequency loaded up to  $2.5 \times 10^2$  Hz. In the frequency range of  $10^3$ – $10^6$  Hz has become similar to all reinforcement loading. This decrease in dielectric permittivity in higher frequency may be accredited to a decrease in the polarization of functionalized MWCNTs.

Figure 11 shows the dielectric loss of PVDF/C-MWCNTs nanocomposites with frequency ranges around  $10^6$  Hz for all loading concentrations. These low values of dielectric loss of PVDF/C-MWCNTs possess low energy loss and thus find practical applications in dielectric materials [27].



**Figure 11.** Relationship of frequency with (a) Dielectric permittivity and (b) Dielectric loss in PVDF/C-MWCNTs nanocomposites.

### 3.7. AC Electrical Conductivity

The AC conductivities of the nanocomposite material with polymeric matrix PVDF/C-MWCNTs/TiO<sub>2</sub> 1%, 3%, and 5% have been measured in the range of  $1 \times 10^1$  Hz to  $1 \times 10^7$  Hz at room temperature, as shown in Figure 12. The conductivity of the materials is independent of the frequency in the case of PVDF/C-MWCNTs/TiO<sub>2</sub>. The samples are showing the independent relation of conductivity with frequency even at the lowest adopted loading (1%). Compared with pure PVDF [28], the independency of conductivity upon different frequencies indicates that the effective conductive network was achieved at 1–5% wt. of the percolation threshold ( $f_c$ ) was attained or loading 1% wt. in PVDF/C-MWCNTs/TiO<sub>2</sub> nanocomposites. The conductivity of materials at frequency of  $1 \times 10^2$  Hz has reached  $6.01 \times 10^{-5}$ ,  $5.1 \times 10^{-4}$ , and  $6.9 \times 10^{-4}$  S/cm for loading samples of 1%, 3%, and 5% wt., respectively. However, the electrical conductivity of PVDF has been observed to increase with the addition of functionalized MWCNTs and titanium oxide as in the increased concentration from 1% to 5% wt. Thus, the conductivity of nanocomposite material has increased linearly with the increasing concentration of filler due to the improvement in their dispersion in PVDF.

This mechanism related the conductivity of charges that was proceeded by tunneling of electrons through insulating gaps of PVDF within nanocomposite [29–32]. This phenomenon was based on the formation of a two-dimensional (2D) network of functionalized MWCNTs in the vicinity of threshold frequency  $f_c$  instead of three-dimensional (3D) conductive networks. The movement of electrons is carried out through matrix via the rule given in the equation:

$$\log_{10} \sigma \propto f_{f-MWCNTs}^{-1/3} \quad (1)$$

Here  $\sigma$  is the conductivity and  $f$  is the fraction of functionalized MWCNTs and TiO<sub>2</sub> in nanocomposites. The  $\log_{10} \sigma$  was plotted against the fraction of functionalized substrate

as shown in figure. The marly linear relationship between the  $\log_{10}\sigma$  and functionalized substrate valued the conductivity through tunneling mechanism, where electrons hop between the conduction zones but CNTs are not contacted physically. The concentration of C-MWCNT/TiO<sub>2</sub> increases, and the formation of the 3D network become prominent and directly contacts it, and thus conductivity increases appreciably. The linear relationship of conductive PVDF with loading material C-MWCNT/TiO<sub>2</sub> was further confirmed through the relationship of the conductivity with reinforcement fraction at  $1 \times 10^2$  Hz, as shown in Figure 13.

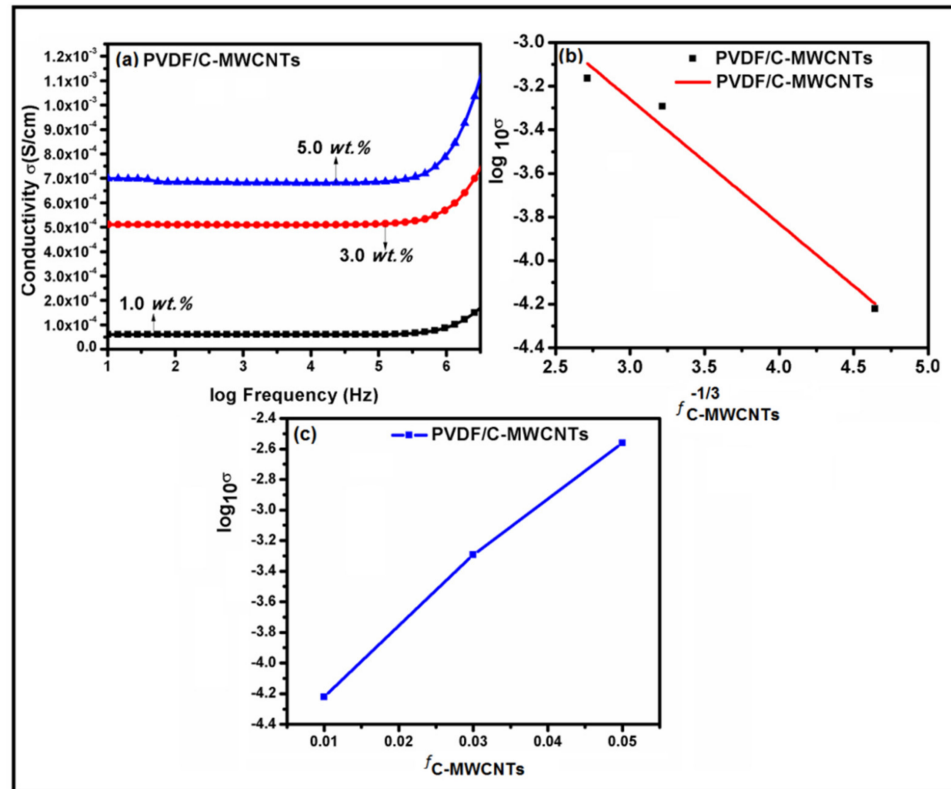


Figure 12. Relationship of (a) AC conductivity vs. log frequency (b) linear fit of the  $\log_{10}\sigma$  vs. frequency and (c)  $\log_{10}\sigma$  vs. fraction of C-MWCNTs.

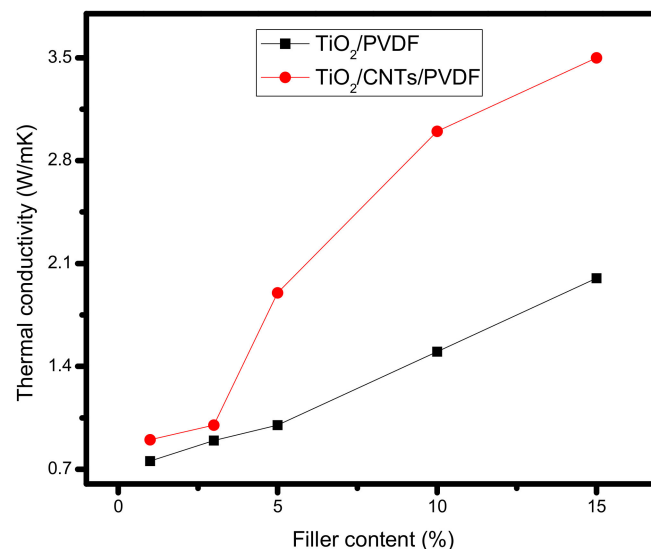


Figure 13. Thermal conductivity analysis for (%) filler content.

The thermal conductivity network has been analyzed for the composite material of PVDF/CNTs/TiO<sub>2</sub> to establish the highest thermal conductivity of the material as shown in Figure 13. However, the filler content of composite material with TiO<sub>2</sub> (1%, 3%, 5%, 10%, and 15%) showed conductivity ranges of between 0.6–2 W/mK, which is increased with the increase in concentration. As the filler content increased the thermal conductivity of the material also increased. The material PVDF/TiO<sub>2</sub> nanowires with a percentage composite 1% to 3% is 0.756 W/mK and 0.896 W/mK respectively while 5% and above have three times greater thermal conductivity. The filler content of PVDF/CNTs/TiO<sub>2</sub> as percentage composite by weight (1%, 3%, 5%, 10%, and 15%) increased their thermal conductivity. The PVDF/CNTs/TiO<sub>2</sub> have a thermal conductivity of 0.932 W/mK, 1.001 W/mK, for 1% and 3% by weight, respectively, whereas 5% and above have five times increased thermal conductivity. While comparing the thermal conductivity of PVDF/TiO<sub>2</sub> nanowires with PVDF/CNTs/TiO<sub>2</sub> change were observed as shown in figure. The result opts to be the encouraging conductive path to develop nanowires of TiO<sub>2</sub>. The electrical conductivity of the composite increases i.e., many orders higher, near the percolation threshold transition point. However, a steep thermal change was not observed. The overall thermal conductivity of the polymeric material is still low, unlike the electrical conductivity of the pure material of metal oxide. In the formulation of the tunneling electron barrier across the polymer, the main carrier of thermal conductivity are photons that do not have a tunneling effect. Hence, the scattering phenomenon results in a large interface thermal resistance and hinders photon transmission. However, at the same loading of PVDF/TiO<sub>2</sub> nanowires with PVDF/CNTs/TiO<sub>2</sub> there is a thermal conductivity increase while adding 1, 3, 5, 10, and 15 wt. % of titanium oxide nanowires that correspond to 0.756, 0.896, 1, 1.467 and 2 W/mK, respectively.

Generally, comprehending the dispersion of conductive fillers in a matrix is fruitful to construct a thermal conductivity network, which enhances the thermal conductive properties of the polymeric matrix. TiO<sub>2</sub> nanowires show a uniform intermediate coated layer to establish the elastic modulus of thin polymeric films of anatase ~185 GPa [33]. The high elastic modulus TiO<sub>2</sub> increases the modulus mismatch between titanium oxide nanowires and polymer [34,35] and expressed the thermal conductivity is higher for uncoated composites as evident. The lower elastic modulus between loading material and polymeric matrix can increase the phonon spectrum overlap and improves the phonon transmission efficiency. Here, PVDF/TiO<sub>2</sub> nanowires with PVDF/CNTs/TiO<sub>2</sub> composite reveal the highest thermal conductivity. The nanowires of TiO<sub>2</sub> can act as a “dispersion agent”, to improve dispersion in the polymeric matrix, resulting in an apparent improvement in thermal conductivity of the polymeric composite. Recently, it was observed that composite Cu nanowires and titanium oxide nanowires with epoxy revealed a thermal conductivity of 1.124 W/mK with 2.0 percent volume [35]. There are many test methods to check the thermal conductivity of the polymeric composite material, such as the hot wire method and the laser flash method. The result measured by applying these two methods shows some noteworthy differences [36]. Therefore, these two methods are not comparable, as the result shows noteworthy differences. Notably, at relatively low filler content, the hot wire method is used for the best results.

#### 4. Conclusions

The synthesis of TiO<sub>2</sub> nanowires via the emulsion electrospinning method plays a significant role in nanotechnology. The addition of CNTs in the membrane accomplishes very attractive features. For analysis, we used FTIR, SEM, EDX, XRD, and TGA techniques to determine the morphology, crystalline geometry, and thermal stability. To check variation, we catered concentration of nanowires in blend membrane which bring variation in membrane with nanowires. SEM analysis revealed nanowire size as well blend with polymeric membrane up to 20 nm for which magnification of the instrument ranges to 50,000 to 1500. The FTIR outcome indicated that the composition of the nanowires of titanium oxide ranges between 600 to 1100 cm<sup>-1</sup>. From an application point of view, the polymeric

membrane with wires is used in many ways, such as in electrochemical sensing, catalysis and photocatalysis, photovoltaics, UV blocking, smart packing, and functional filler in textiles, paints, paper, and cosmetics, due to their special electrical, optical properties and dielectric applications that are of significant importance.

**Author Contributions:** Conceptualization, M.A.D., Z.U.R., M.N. and H.U.; methodology, M.A.D., H.U. and M.I.; software, S.H. and P.A.; validation, P.A. and M.U.K.; formal analysis, M.A.D. and Z.U.R.; investigation, H.U.; resources, H.U. and M.U.K.; data curation, P.A. and N.T.; writing—original draft preparation, M.A.D., Z.U.R. and M.I.; writing—review and editing, S.H., N.T. and A.S.; visualization, H.U. and M.A.B.; supervision, M.N. and S.H.; project administration, M.N.; funding acquisition, N.T. and A.S. All authors have read and agreed to the published version of the manuscript.

**Funding:** The authors express their gratitude to Princess Nourah bint Abdulrahman University Researchers Supporting Project (Grant No. PNURSP2022R12), Princess Nourah bint Abdulrahman University, Riyadh, Saudi Arabia.

**Institutional Review Board Statement:** Not Applicable.

**Informed Consent Statement:** Not Applicable.

**Data Availability Statement:** All the data available within the manuscript.

**Conflicts of Interest:** The authors declare that they have no conflict of interest.

## References

1. Hong, S.; Liow, C.H.; Yuk, J.M.; Byon, H.R.; Yang, Y.; Cho, E.; Yeom, J.; Park, G.; Kang, H.; Kim, S.; et al. Reducing Time to Discovery: Materials and Molecular Modeling, Imaging, Informatics, and Integration. *ACS Nano* **2021**, *15*, 3971–3995. [[CrossRef](#)] [[PubMed](#)]
2. Liu, G.; Zhang, X.; Chen, X.; He, Y.; Cheng, L.; Huo, M.; Yin, J.; Hao, F.; Chen, S.; Wang, P.; et al. Additive manufacturing of structural materials. *Mater. Sci. Eng. R Rep.* **2021**, *145*, 100596. [[CrossRef](#)]
3. Yadav, P.K.; Ajitha, B.; Reddy, Y.A.K.; Sreedhar, A. Recent advances in development of nanostructured photodetectors from ultraviolet to infrared region: A review. *Chemosphere* **2021**, *279*, 130473. [[CrossRef](#)] [[PubMed](#)]
4. Nehra, M.; Dilbaghi, N.; Marrazza, G.; Kaushik, A.; Abolhassani, R.; Mishra, Y.K.; Kim, K.H.; Kumar, S. 1D semiconductor nanowires for energy conversion, harvesting and storage applications. *Nano Energy* **2020**, *76*, 104991. [[CrossRef](#)]
5. Wang, D.; Wang, L.; Shen, G. Nanofiber/nanowires-based flexible and stretchable sensors. *J. Semicond.* **2020**, *41*, 041605. [[CrossRef](#)]
6. Altaf, A.A.; Ahmed, M.; Hamayun, M.; Kausar, S.; Waqar, M.; Badshah, A. Titania nano-fibers: A review on synthesis and utilities. *Inorganica Chim. Acta* **2019**, *501*, 119268. [[CrossRef](#)]
7. Zhao, L.; Duan, G.; Zhang, G.; Yang, H.; He, S.; Jiang, S. Electrospun Functional Materials toward Food Packaging Applications: A Review. *Nanomaterials* **2020**, *10*, 150. [[CrossRef](#)]
8. Huang, C.; Thomas, N.L. Fabrication of porous fibers via electrospinning: Strategies and applications. *Polym. Rev.* **2019**, *60*, 595–647. [[CrossRef](#)]
9. Pereira, C.; Pereira, A.M.; Freire, C.; Pinto, T.V.; Costa, R.S.; Teixeira, J.S. Nanoengineered textiles: From advanced functional nanomaterials to groundbreaking high-performance clothing. In *Handbook of Functionalized Nanomaterials for Industrial Applications*; Elsevier: Amsterdam, The Netherlands, 2020; pp. 611–714.
10. Fattakhova-Rohlfing, D.; Zaleska, A.; Bein, T. Three-Dimensional Titanium Dioxide Nanomaterials. *Chem. Rev.* **2014**, *114*, 9487–9558. [[CrossRef](#)]
11. Sun, M.-H.; Huang, S.-Z.; Chen, L.-H.; Li, Y.; Yang, X.-Y.; Yuan, Z.-Y.; Su, B.-L. Applications of hierarchically structured porous materials from energy storage and conversion, catalysis, photocatalysis, adsorption, separation, and sensing to biomedicine. *Chem. Soc. Rev.* **2016**, *45*, 3479–3563. [[CrossRef](#)]
12. Liu, L.; Ma, W.; Zhang, Z. Macroscopic Carbon Nanotube Assemblies: Preparation, Properties, and Potential Applications. *Small* **2011**, *7*, 1504–1520. [[CrossRef](#)] [[PubMed](#)]
13. Ahmed, S.; Cai, Y.; Ali, M.; Khanal, S.; Xu, S. Preparation and performance of nanoparticle-reinforced chitosan proton-exchange membranes for fuel-cell applications. *J. Appl. Polym. Sci.* **2018**, *136*, 46904. [[CrossRef](#)]
14. Ahmed, S.; Cai, Y.; Ali, M.; Khannal, S.; Ahmad, Z.; Lu, Y.; Wang, S.; Xu, S. One-step phosphorylation of graphene oxide for the fabrication of nanocomposite membranes with enhanced proton conductivity for fuel cell applications. *J. Mater. Sci. Mater. Electron.* **2019**, *30*, 13056–13066. [[CrossRef](#)]
15. Ahmed, S.; Cai, Y.; Ali, M.; Khannal, S.; Xu, S. Preparation and properties of alkyl benzene sulfonic acid coated boehmite/chitosan nanocomposite membranes with enhanced proton conductivity for proton exchange membrane fuel cells. *Mater. Express* **2019**, *9*, 42–50. [[CrossRef](#)]
16. Hassan, M.; Afzal, A.; Tariq, M.; Ahmed, S. Synthesis of the hyper-branched polyamides and their effective utilization in adsorption and equilibrium isothermal study for cadmium ion uptake. *J. Polym. Res.* **2021**, *28*, 1–11. [[CrossRef](#)]



17. Ahmed, S.; Arshad, T.; Zada, A.; Afzal, A.; Khan, M.; Hussain, A.; Hassan, M.; Ali, M.; Xu, S. Preparation and characterization of a novel sulfonated titanium oxide incorporated Chitosan nanocomposite membranes for fuel cell application. *Membranes* **2021**, *11*, 450. [[CrossRef](#)]
18. Chae, S.R.; Yamamura, H.; Ikeda, K.; Watanabe, Y. Effect of pre-treatment on membrane fouling of PVDF (Polyvinylidene Fluoride) microfiltration membrane with different structures in a pilot-scale drinking water production system. *Water Res.* **2008**, *42*, 2029–2042. [[CrossRef](#)]
19. Park, H.H.; Deshwal, B.R.; Jo, H.D.; Choi, W.K.; Kim, I.W.; Lee, H.K. Absorption of nitrogen dioxide by PVDF hollow fiber membranes in a G–L contactor. *Desalination* **2009**, *243*, 52–64. [[CrossRef](#)]
20. Sessler, G. Piezoelectricity in polyvinylidene fluoride. *J. Acoust. Soc. Am.* **1981**, *70*, 1596–1608. [[CrossRef](#)]
21. Seminara, L.; Capurro, M.; Cirillo, P.; Cannata, G.; Valle, M. Electromechanical characterization of piezoelectric PVDF polymer films for tactile sensors in robotics applications. *Sens. Actuators A Phys.* **2011**, *169*, 49–58. [[CrossRef](#)]
22. Bensouici, F.; Souier, T.; Dakhel, A.; Iratni, A.; Tala-Ighil, R.; Bououdina, M. Synthesis, characterization and photocatalytic behavior of Ag doped TiO<sub>2</sub> thin film Superlattices. *Microstruct* **2015**, *85*, 255–265. [[CrossRef](#)]
23. Sahoo, N.G.; Rana, S.; Cho, J.W.; Li, L.; Chan, S.H. Polymer nanocomposites based on functionalized carbon nanotubes. *Prog. Polym. Sci.* **2010**, *35*, 837–867. [[CrossRef](#)]
24. Kakanakova-Georgieva, A.; Gueorguiev, G.; Sangiovanni, D.G.; Suwannaharn, N.; Ivanov, I.G.; Cora, I.; Pécz, B.; Nicotra, G.; Giannazzo, F. Nanoscale phenomena ruling deposition and intercalation of AlN at the graphene/SiC interface. *Nanoscale* **2020**, *12*, 19470–19476. [[CrossRef](#)] [[PubMed](#)]
25. Santos, D.R.B.; Rivelino, R.; Gueorguiev, G.K.; Kakanakova-Georgieva, A. Exploring 2D structures of indium oxide of different stoichiometry. *CrystEngComm* **2021**, *23*, 6661–6667. [[CrossRef](#)]
26. Li, C.; Thostenson, E.T.; Chou, T.-W. Dominant role of tunneling resistance in the electrical conductivity of carbon nanotube-based composites. *Appl. Phys. Lett.* **2007**, *91*, 223114. [[CrossRef](#)]
27. Eitan, A.; Jiang, K.; Dukes, D.; Andrews, A.R.; Schadler, L.S. Surface Modification of Multiwalled Carbon Nanotubes: Toward the Tailoring of the Interface in Polymer Composites. *Chem. Mater.* **2003**, *15*, 3198–3201. [[CrossRef](#)]
28. Roach, P.; Shirtcliffe, N.J.; Newton, M.I. Progress in superhydrophobic surface development. *Soft Matter* **2007**, *4*, 224–240. [[CrossRef](#)]
29. Hassan, M.; Abbas, G.; Li, N.; Afzal, A.; Haider, Z.; Ahmed, S.; Xu, X.; Pan, C.; Peng, Z. Significance of Flexible Substrates for Wearable and Implantable Devices: Recent Advances and Perspectives. *Adv. Mater. Technol.* **2021**, *7*, 2100773. [[CrossRef](#)]
30. Al-Saleh, M.H.; Sundararaj, U. A review of vapor grown carbon nanofiber/polymer conductive composites. *Carbon* **2009**, *47*, 2–22. [[CrossRef](#)]
31. Yu, H.; Huang, T.; Lu, M.; Mao, M.; Zhang, Q.; Wang, H. Enhanced power output of an electrospun PVDF/MWCNTs-based nanogenerator by tuning its conductivity. *Nanotechnology* **2013**, *24*, 405401. [[CrossRef](#)]
32. Anderson, O.; Ottermann, C.R.; Kuschnerit, R.; Hess, P.; Bange, K. Density and Young's modulus of thin TiO<sub>2</sub> films. *Anal. Bioanal. Chem.* **1997**, *358*, 315–318. [[CrossRef](#)]
33. Mayo, M.J.; Siegel, R.W.; Narayanasamy, A.; Nix, W.D. Mechanical properties of nanophase TiO<sub>2</sub> as determined by nanoindentation. *J. Mater. Res.* **1990**, *5*, 1073–1082. [[CrossRef](#)]
34. Wu, B.; Heidelberg, A.; Boland, J.J.; Sader, J.E.; Sun, X.M.; Li, Y.D. Microstructure-hardened silver nanowires. *Nano Lett.* **2006**, *6*, 468–472. [[CrossRef](#)] [[PubMed](#)]
35. Ahn, K.; Kim, K.; Kim, J. Thermal conductivity and electric properties of epoxy composites filled with TiO<sub>2</sub>-coated copper nanowire. *Polymer* **2015**, *76*, 313–320. [[CrossRef](#)]
36. Han, Z.D.; Fin, A. Thermal conductivity of carbon nanotubes and their polymer nanocomposites: A review. *Prog. Polym. Sci.* **2011**, *36*, 914–944. [[CrossRef](#)]